

# Netcast: Low-Power Edge Computing with WDM-defined Optical Neural Networks

Ryan Hamerly, *Member, Optica*, Alexander Sludds, *Student Member, Optica*, Saumil Bandyopadhyay, Zaijun Chen, Zhizhen Zhong, *Member, Optica*, Liane Bernstein, Dirk Englund, *Member, IEEE*

**Abstract**—This paper analyzes the performance and energy efficiency of Netcast, a recently proposed optical neural-network architecture designed for edge computing. Netcast performs deep neural network inference by dividing the computational task into two steps, which are split between the (cloud) server and (edge) client: (1) the server employs a wavelength-multiplexed modulator array to encode the network's weights onto an optical signal in an analog time-wavelength basis, and (2) the client obtains the desired matrix-vector product through modulation and time-integrated detection. The simultaneous use of wavelength multiplexing, broadband modulation, and integration detection allows large neural networks to be run at the client by effectively pushing the energy and memory requirements back to the server. The performance and energy efficiency are fundamentally limited by crosstalk and detector noise, respectively. We derive analytic expressions for these limits and perform numerical simulations to verify these bounds.

**Index Terms**—Edge computing, split computing, neural networks, WDM.

## I. INTRODUCTION

MACHINE learning is widespread in the cloud, where ample processing power is co-located with data, but in recent years, network and privacy constraints have pushed processing closer to the end user [1]. This “edge computing” paradigm introduces new constraints to hardware and software design, as data processing happens on size, weight and power (SWaP)-constrained devices at the edge of the network. In light of the growing importance of deep neural networks (DNNs) in information processing, significant effort has been dedicated to SWaP-constrained hardware [2], [3] and algorithms [4]–[7] for DNN edge inference. While these efforts have enabled edge deployment of intermediate-size neural networks [8], many state-of-the-art DNNs are still too large [9], [10] to be efficiently run on the edge.

Consequently, edge computing is a prime target for emerging hardware technologies. Memristive circuits [11] are a leading candidate, leveraging the standard electronics process as well as the substantial body of work towards edge inference on memristor crossbar arrays. However, practical issues of uniformity, accuracy, and resistance updates remain outstanding challenges for the field [12]; moreover, the weight stationary [2] character of memristor networks means SWaP constraints

will still set an upper limit on the DNN size, and will limit the frequency of network updates. Photonic architectures have also gained traction, owing to the physical mapping between matrix-vector multiplication (the hardware bottleneck in DNN inference [2]) and linear-optical processes. However, scaling issues are much more pronounced in photonics, and usually involve a tradeoff between speed, size, and programmability [13]–[19]. Moreover, in integrated architectures, chip area constraints, loss, and error propagation [20]–[25] make large networks especially challenging to implement.

Recently, we introduced Netcast, an optical neural network architecture that combines the advantages of wavelength division multiplexing (WDM), broadband modulation, and integration detection [26]–[28]. Our protocol consists of two components: a WDM modulator array (server), which is connected by an optical link to the SWaP-constrained edge device (client) which consists of a single modulator, a demultiplexer, and a set of time-integrating detectors. For each DNN layer, over a sequence of time steps, the server encodes the weight matrix as an analog optical waveform, with matrix elements stored in a time-wavelength basis. At the client, this signal is modulated and demultiplexed, and the charge accumulated on the detectors encodes the neuron activations for the next DNN layer. Netcast leverages the high bandwidth of WDM optical links to effectively “split” the computation into two parts, pushing the hard part of the computation to the server while the client only performs a minimal postprocessing step. This enables low-power DNN edge inference for large networks that would otherwise be infeasible due to power or memory constraints of edge devices. In this paper, we analyze the limits to the performance and energy consumption of Netcast, which are set by crosstalk and detector noise, respectively. We derive analytic expressions for these bounds, which are verified with numerical simulations.

## II. NETCAST CONCEPT

Fig. 1 illustrates the concept. The architecture consists of a *server* and a *client*, connected by an optical *link*. Since linear algebra is the bottleneck step for DNN inference and training, we focus on how the optical hardware accelerates matrix-vector multiplication (MVM)  $y_m = \sum_n w_{mn}x_n$  at the client; the nonlinear activation function, pooling, and batch normalization can be performed digitally at the client with minimal added cost. In the output-stationary dataflow [2], an  $M \times N$  MVM is performed in  $N$  time steps, where in each step a column of the weight matrix  $w$  is weighted by an element of

R.H., A.S., S.B., Z.C., L.B., and D.E. are with MIT Research Laboratory of Electronics, Cambridge, MA 02139, USA

R.H. and S.B. are with NTT Research Inc., Physics & Informatics Laboratories, Sunnyvale, CA 94085, USA

Z.Z. is with MIT Computer Science and Artificial Intelligence Laboratory, Cambridge, MA 02139, USA

Manuscript received May 16, 2024.

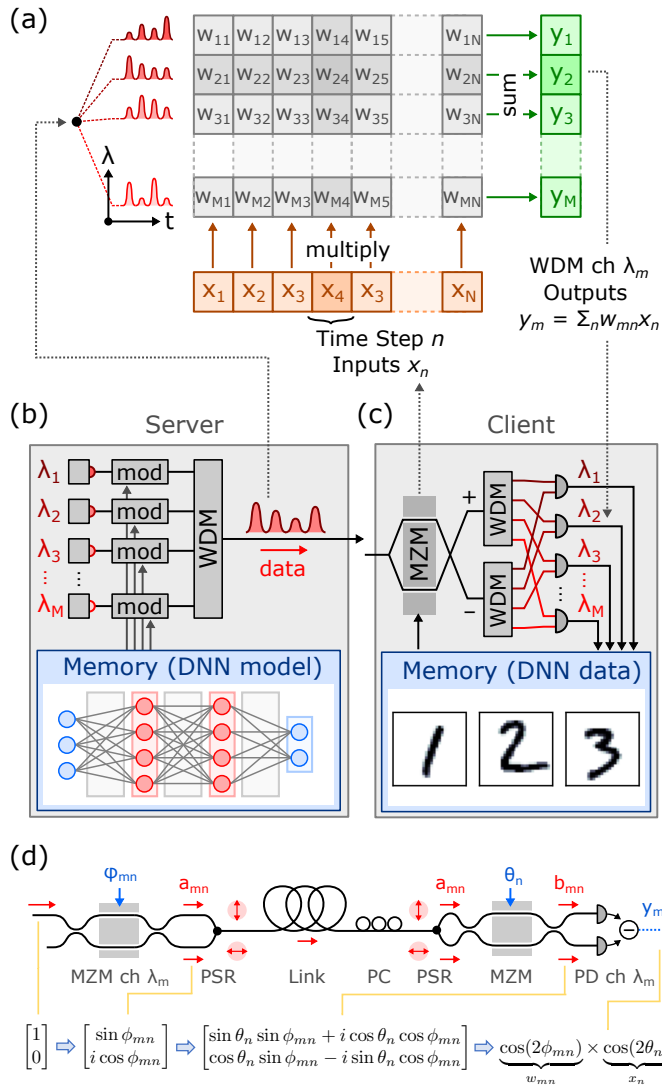


Fig. 1. Schematic of Netcast architecture. (a) Output-stationary dataflow for MVM. At each time step, a column  $w_{:,n}$  is scaled by  $x_n$  and accumulated to the partial sums for  $y_m$ . (b) Weight server consisting of a WDM bank of optical modulators and a large memory containing the full DNN model. (c) Client consisting of a single broadband modulator (e.g. balanced MZM), demultiplexing optics, and integrating detectors. (d) Optical dataflow for a single wavelength channel ( $\lambda_m$ , WDM not shown) in the specific case where modulation is performed with balanced MZMs. The values of the input,  $\vec{a}_{mn}$ ,  $\vec{b}_{mn}$ , and  $y_m$  (up to proportionality constants) are given below.

the activation vector  $x$  and accumulated to the partial sums for  $y$ , i.e.  $y[m] += w[m, n] * x[n]$  (Fig. 1(a)). To perform this operation optically, weight data is encoded in an  $N$ -step pulse train over  $M$  wavelength channels, with the rows and columns of the matrix represented by time and wavelength, respectively. This optical signal can be generated using a WDM modulator bank as shown in Fig. 1(b). At each time step (indexed by  $n$ ), the client receives a column  $w_{:,n}$  of the weight matrix, and modulates this signal using a broadband modulator in order to scale the column by  $x_n$ . The resulting output is demultiplexed into an array of  $M$  balanced detector pairs (one per wavelength) as shown in Fig. 1(c), which produce the products  $w_{mn}x_n$ . Integrating over all  $N$  time steps, the charge

accumulated on the detectors yields the MVM output.

To understand this scheme quantitatively, Fig. 1(d) traces the protocol in more detail. Here, we consider only the path of a single wavelength channel  $\lambda_m$ , since the channels process data independently (but see Sec. V). For concreteness, we employ a balanced Mach-Zehnder modulator (MZM) at both the server and client. The server-side MZM (followed by a  $90^\circ$  phase shift) splits the input into two channels with amplitudes  $\vec{a}_{mn} \equiv (a_{mn}^{(+)}, a_{mn}^{(-)})$ , given by:

$$\vec{a}_{mn} \propto \begin{bmatrix} 1 & 0 \\ 0 & i \end{bmatrix} \underbrace{\begin{bmatrix} \sin \phi_{mn} & \cos \phi_{mn} \\ \cos \phi_{mn} & -\sin \phi_{mn} \end{bmatrix}}_{T(\phi_{mn})} \begin{bmatrix} 1 \\ 0 \end{bmatrix} = \begin{bmatrix} \sin \phi_{mn} \\ i \cos \phi_{mn} \end{bmatrix} \quad (1)$$

which encode the weight through differential signaling  $w_{mn} = |a_{mn}^{(+)}|^2 - |a_{mn}^{(-)}|^2$  (analogous to the weight banks of Ref. [17]). Next, a polarization splitter/rotator (PSR) [29] combines the through- and drop-port outputs to the orthogonal polarizations of the optical link, where the signal is transmitted to the client. Links may be over fiber or free space (e.g. using techniques from WDM free-space communications [30], [31]), and may include optical fan-out to multiple clients. If the link loss or fan-out ratio is large, the server output can be pre-amplified.

At the end of the link, the signal enters the client (Fig. 1(d), right), where a second PSR (after any necessary polarization control (PC)) separates the polarizations and a phase shifter is used to correct for any relative phase shift accrued in the link, effectively recovering the signal pair  $\vec{a}_{mn}$  from before the server-side PSR. These inputs are scrambled using a two-port broadband MZM, whose voltage encodes the current activation  $x_n$ . At the output of this MZM we have:

$$\vec{b}_{mn} = T(\theta_n) \vec{a}_{mn} \propto \begin{bmatrix} \sin \theta_n \sin \phi_{mn} + i \cos \theta_n \cos \phi_{mn} \\ \cos \theta_n \sin \phi_{mn} - i \sin \theta_n \cos \phi_{mn} \end{bmatrix} \quad (2)$$

Finally, the WDM channels are demultiplexed and the power in each channel is read out on a photodetector. We care about the differential charge accumulated between the MZM outputs, integrated over  $N$  time steps, which evaluates to:

$$Q_m \propto \sum_n [ |b_{mn}^{(+)}|^2 - |b_{mn}^{(-)}|^2 ] \propto \sum_n \underbrace{\cos(2\phi_{mn})}_{\text{input } w_{mn}} \times \underbrace{\cos(2\theta_n)}_{\text{input } x_n} \quad (3)$$

In this way, for the inputs and weights scaled to the range  $x_n, w_{mn} \in [-1, +1]$ , and encodings  $\phi_{mn} = \frac{1}{2} \cos^{-1}(w_{mn})$  and  $\theta_n = \frac{1}{2} \cos^{-1}(x_n)$ , the charge accumulated at the detector pair is proportional to  $y_m$ , performing the desired MVM.

While Eq. (3) is specific to MZMs, the Netcast architecture is compatible with a range of modulators, subject to the constraint that the client-side modulator be optically broadband. For example, micro-ring resonators (MRRs) are a particularly compact, scalable, and low-energy (server-side) modulator type [32]–[36]. While MRRs are often deemed unsuitable for high-precision modulation, recent demonstrations of MRR control up to 9 bits of precision [37] highlight the potential for this platform (although the precision at high-speed operation is often lower [38], [39]). In a two-port MRR critically coupled to the input port (with through- and drop-port couplings  $\kappa_1$

and  $\kappa_2$ , satisfying  $\kappa_1 = \kappa_2 + \kappa_{\text{abs}}$ , and a programmable detuning  $\Delta_{mn}$ , the same analysis leading to Eqs. (1-3) yields  $Q_m \propto (\Delta_{mn} - \kappa_1 \kappa_2) / (\Delta_{mn} - \kappa_1^2) \times \cos(2\theta_n)$ . If weights in the range  $w_{mn} \in [-\kappa_2/\kappa_1, +1]$  are encoded into the MRR detuning as  $\Delta_{mn} = \kappa_1 \sqrt{(\kappa_2/\kappa_1 + w_{mn}) / (1 - w_{mn})}$ , then the charge  $Q_m$  will yield the desired matrix-vector product.

The main insight underlying Netcast is not that photonics provides a means to add and multiply numbers, but that we can (1) perform many operations in parallel and (2) separate the tasks of logic (client) and memory access (server) by means of an optical link. Although the server and client cooperate to perform the calculation, the workloads are unequal, and for large DNNs, the energy and memory costs at the client are significantly lower than those at the server:

- For a layer of size  $N \times N$ , the memory cost scales as  $O(N^2)$  at the server and  $O(N)$  at the client. In general, memory reads (especially from off-chip DRAM) dominate the energy consumption in DNN hardware [2]. Additionally, the server must drive  $N$  modulators for a total energy cost of  $O(N^2)$ , while the client only drives a single modulator. The client reads out  $N$  detectors, but only after time-integration ( $O(N)$  cost).
- The server stores the full neural network, giving a memory requirement of  $O(N^2 L)$ , where  $L$  is the number of layers; by contrast, the client stores only the activations, which requires a much smaller memory of size  $O(N)$ —consistent with the general observation in neuroscience that the ratio of synapses to neurons is very large.
- Although the client-side energy cost only scales as  $O(N)$ , the client performs the full  $N^2$  operations for an MVM. The broad optical bandwidth of a balanced MZM, which can simultaneously modulate optical signals at multiple wavelengths [27], [40], coupled with the use of integrating detectors [41], allows the client to leverage an  $O(N)$  optical parallelism factor [42], reducing the client-side MVM cost from quadratic to linear scaling.

By means of a single-mode optical link, the Netcast scheme pushes all of the difficult parts of the computation to the server, liberating the edge client from a significant part of its SWaP constraints. This can in principle enable the edge deployment of entirely new classes of DNNs that have up to now been restricted to use in data centers.

### III. VARIATIONS

The key concepts of Netcast—WDM, parallel modulation, and integration detection—admit a number of variations, the most obvious ones depicted in Fig. 2. All of these schemes encode the weight matrix in time-frequency (i.e. time-wavelength) space, where  $w_{mn}$  is the amplitude of wavelength band  $\lambda_m$  at time step  $t_n$ . Two matrix-vector multiplications are possible (Fig. 2(a)): right-multiplication  $y = wx$  through Time Integration / Frequency Separation (TIFS), or left-multiplication  $y^T = x^T w$  through Frequency Integration / Time Separation (FITS). The system presented in Fig. 1 used TIFS. For FITS, the client uses a weight bank (WB) [17] consisting of an array of ring resonators, which integrates over frequency with the activations  $x_m$  encoded in

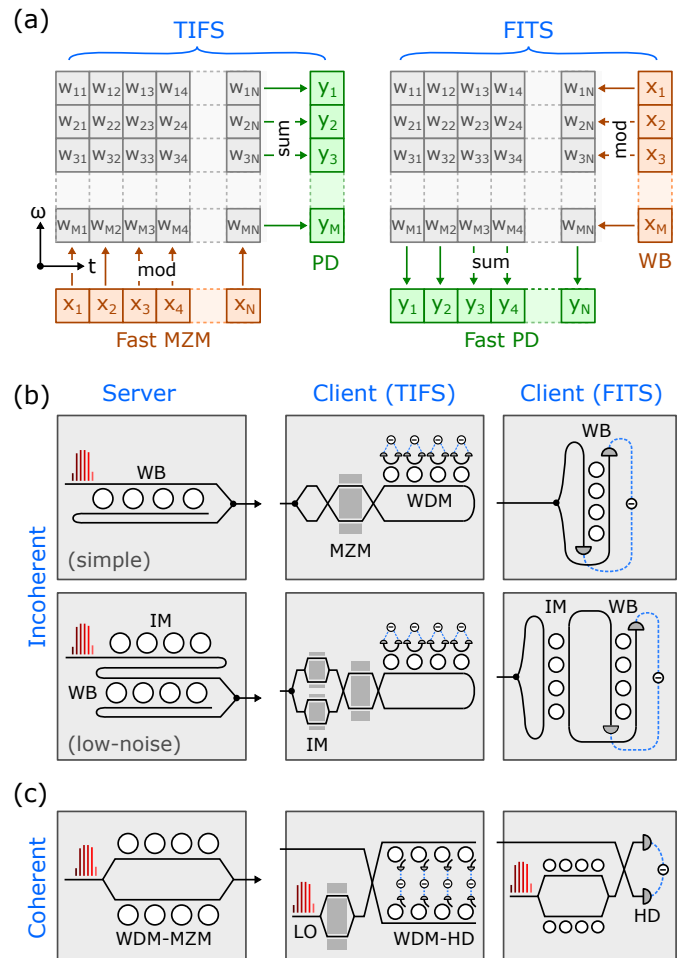


Fig. 2. Variants of optical implementation. (a) MVM implemented by time integration / frequency separation (left) and frequency integration / time separation (right). (b) Server and client architectures for incoherent encoding. Here a WDM ring array is depicted for the server modulators. One can mix and match server and client designs. (c) Coherent encoding architectures.

the resonator detunings (Fig. 2(b-c)). Time separation requires a single fast detector pair, unlike the TIFS schemes where  $M$  slow detectors are used. In both cases,  $M$  signals must be detected and digitized per MVM. The choice of architecture (TIFS or FITS) will be a tradeoff involving the fixed and variable power costs of the client modulator, driver, detector, and readout circuitry.

Another distinction is the modulation format. The approach in Fig. 1 shows the simplest case: incoherent differential signaling with fixed power. However, for small differential signals, shot noise can present a challenge to this approach, but with additional hardware complexity at either the server or client, one can lower this receiver noise (Fig. 2(b), Sec. III-A). Additionally, with a client-side local oscillator, one can encode the signal coherently, which increases bandwidth and reduces noise to the quantum limit (Fig. 2(c), Sec. III-B). Altogether, this leads to  $2^2 \times 2 + 1^2 \times 2 = 10$  possibilities.

TABLE I

COMPARISON OF THE FOUR INCOHERENT SCHEMES AND THE COHERENT SCHEME. <sup>†</sup>WEIGHT AND PD INPUT PHOTON NUMBERS FOR CASE  $w_{mn} > 0$ ,  $x_n > 0$  SHOWN. THE OTHER CASES ARE ANALOGOUS AND THE FORMS FOR  $Q_{\text{tot}}$ ,  $Q_{\text{diff}}$  ARE THE SAME.

Scheme	Transmitter <sup>†</sup>		Detector <sup>†</sup>			Noise	
	$ a_{\pm} ^2/N_{\text{src}}$	$N_{\text{tr}}/N_{\text{src}}$	$ b_{\pm} ^2/N_{\text{src}}$	$Q_{\text{diff}}/N_{\text{src}}$	$Q_{\text{tot}}/N_{\text{src}}$	$F_{\text{src}}$	$F_{\text{tr}}$
S/S	$\frac{1}{2}(1 \pm w_{mn})$	1	$\frac{1}{2}(1 \pm w_{mn}x_n)$	$w_{mn}x_n$	1	1	1
S/LN	$\frac{1}{2}(1 \pm w_{mn})$	1	$\frac{1}{2}(1 \pm w_{mn})x_n$	$w_{mn}x_n$	$ x_n $	$\langle  x_n  \rangle$	$\langle  x_n  \rangle$
LN/S	$\{w_{mn}, 0\}$	$\langle  w_{mn}  \rangle$	$\frac{1}{2}w_{mn}(1 \pm x_n)$	$w_{mn}x_n$	$ w_{mn} $	$\langle  w_{mn}  \rangle$	$\langle  w_{mn}  \rangle^2$
LN/LN	$\{w_{mn}, 0\}$	$\langle  w_{mn}  \rangle$	$\{w_{mn}x_n, 0\}$	$w_{mn}x_n$	$ w_{mn}x_n $	$\langle  w_{mn}x_n  \rangle$	$\langle  w_{mn}  \rangle \langle  w_{mn}x_n  \rangle$
Coherent	$a_{\text{wt}} = w_{mn}\alpha_{\text{src}}$	$\langle  w_{mn} ^2 \rangle$	$\frac{1}{2}(\alpha_x x_n \pm \alpha_{\text{src}} w_{mn})^2$	$2\alpha_x \alpha_{\text{src}} w_{mn}x_n$	$\alpha_x^2  x_n ^2$	$\frac{1}{4} \langle  x_n ^2 \rangle$	$\frac{1}{4} \langle  w_{mn} ^2 \rangle \langle  x_n ^2 \rangle$

### A. Differential Noise Reduction for Incoherent Netcast

As noted, a critical challenge to the simple differential detection scheme of Fig. 1(d) is the poor signal-to-noise ratio for small inputs, since the shot noise is proportional to the total charge  $Q_{\text{tot}} \propto [|b_{mn}^{(+)}|^2 + |b_{mn}^{(-)}|^2]$ , which is a constant. Therefore, to resolve a signal of order  $\epsilon \ll 1$ , the receiver requires  $O(1/\epsilon^2)$  photons to beat the shot noise. In realistic DNNs, many weights are small or pruned to zero, so in order to obtain a reasonable signal-to-noise ratio, unacceptably high optical powers may be required. We refer to this as the case of “simple” differential signaling (denoted S). To circumvent the problem of shot noise, one can prepend an intensity modulator to the server or client (Fig. 2(b)), creating a “low-noise” device (denoted LN) where differential signaling on small signals uses small total optical powers, greatly reducing the shot noise.

To show the advantage of the “low-noise” configurations, here we consider the four cases, named S/S, S/LN, LN/S, LN/LN (simple server / simple client, etc.). In all cases, we start with an unweighted WDM light source with amplitudes  $\alpha_w$ , where  $N_{\text{src}} = |\alpha_w|^2$  is the number of photons per weight (at the source), and normalize variables so that  $w, x \in [-1, 1]$ .

- 1) *S/S*: The weight bank (WB) encodes  $w_{mn}$  into the differential power in two channels, multiplexed with a PSR (Fig. 2(b), top). These are  $|a_{\pm}|^2 = \frac{1}{2}(1 \pm w_{mn})N_{\text{src}}$  (for the rest of this section, we omit indices  $(m, n)$  of  $a_{\pm}$ ,  $b_{\pm}$  for clarity). At the client these channels are mixed with the MZM to give  $|b_{\pm}|^2 = \frac{1}{2}(1 \pm w_{mn}x_n)N_{\text{src}}$ . Thus the differential charge is  $Q_{\text{diff}} = |b_+|^2 - |b_-|^2 = w_{mn}x_n N_{\text{src}}$ , while the total absorbed charge, which sets the shot noise, is  $Q_{\text{tot}} = |b_+|^2 + |b_-|^2 = N_{\text{src}}$ .
- 2) *S/LN*: Here we use the same inputs as S/S, but the client has an additional pair of intensity modulators (IM) before the MZM (Fig. 2(b), lower center / right). The IMs attenuate the power according to the amplitude  $|x_n|$ , while the MZM works in binary mode to encode the sign ( $\theta_n = \arg(x_n) \in \{0, \pi/2\}$ ). Thus the PD input is either  $|b_{\pm}|^2 = \frac{1}{2}(1 \pm w_{mn})|x_n|N_{\text{src}}$  for  $x_n > 0$ , or  $\frac{1}{2}(1 \mp w_{mn})|x_n|N_{\text{src}}$  for  $x_n < 0$ .  $Q_{\text{diff}}$  is the same, but  $Q_{\text{tot}} = N_{\text{src}}|x_n|$  is reduced by a factor of  $|x_n|$ .
- 3) *LN/S*: In this case, a standard client is used but the weight server has an additional IM before the WB (Fig. 2(b), lower left). Like the S/LN case, the server IM encodes the amplitude  $|w_{mn}|$  while the WB functions in binary mode to encode the sign. Thus, only a single polarization carries power:  $a_+ = |w_{mn}|N_{\text{src}}$  if

$w_{mn} > 0$ , and  $a_- = |w_{mn}|N_{\text{src}}$  if  $w_{mn} < 0$ . The PD input is  $|b_{\pm}|^2 = \frac{1}{2}|w_{mn}|(1 \pm \text{sign}(w_{mn})x_n)N_{\text{src}}$ , which gives the same  $Q_{\text{diff}}$ , but  $Q_{\text{tot}}$  is reduced by a factor of  $|w_{mn}|$  compared to the S/S case.

- 4) *LN/LN*: If both server and client use the low-noise designs, all the power ends up in one of the detectors. This is the most efficient case: either  $|b_+|^2 = |w_{mn}x_n|N_{\text{src}}$  when  $w_{mn}x_n > 0$ , or  $|b_-|^2 = |w_{mn}x_n|N_{\text{src}}$  when  $w_{mn}x_n < 0$ . Thus  $Q_{\text{tot}}$  is reduced by a factor  $|w_{mn}x_n|$ .

These cases are enumerated in Table I. Here we list the transmitter-side amplitudes  $a_{\pm}$  and the corresponding transmitted photon number  $N_{\text{tr}} = |a_+|^2 + |a_-|^2$ , as well as the detector-side amplitudes  $b_{\pm}$ , the measured differential charge  $Q_{\text{diff}} = |b_+|^2 - |b_-|^2$ , and the total charge  $Q_{\text{tot}} = |b_+|^2 + |b_-|^2$ . The important point is that, while they collect the same differential charge  $Q_{\text{diff}} = w_{mn}x_n N_{\text{src}}$ , the total PD charge  $Q_{\text{tot}}$ , which sets the shot-noise limit, can be reduced considerably if many of the  $x_n$  or  $w_{mn}$  are small (or zero).

### B. Netcast with Coherent Detection

By analogy to Ref. [41], one can also construct a coherent version of Netcast, depicted in Fig. 2(c). As in the original scheme (Fig. 1), the weights  $w_{mn}$  are generated at a server in a time-wavelength basis by modulating the lines of a WDM source, and this signal is broadcasted to the client over an optical link. Here we encode data in the complex amplitude of the field rather than its power, and only use a single polarization. To measure this amplitude, we need an identical local oscillator (LO) at the client side. Because of the large number of wavelength channels, a frequency comb may be the ideal source at both server and client; comb locking remains an active topic in telecommunications research [43]–[46]. A fraction of the LO power (not shown) is mixed with the signal to generate a beatnote in order to lock the LO comb to the server. The remainder is amplitude modulated in an MZM, which scales the LO amplitude by the activations  $x_n$ . A wavelength-demultiplexed homodyne detector accumulates the products  $w_{mn}x_n$ , which integrate out to give the matrix-vector product just as in the incoherent case.

One advantage of the coherent scheme is bandwidth: with IQ modulation, one can encode information on both quadratures simultaneously. Moreover, the coherent encoding requires only a single polarization (unlike the differential-signaling scheme of Fig. 1(d)), so both polarizations can carry independent data streams. Taken together, these degrees

of freedom give a  $4\times$  higher data rate than the incoherent scheme (a similar bandwidth leap is observed when moving to coherent formats in telecommunications [47]). In addition, the coherent scheme benefits from increased SNR, especially at low signal powers. This is especially relevant for long-distance free-space links where the transmission efficiency is very low. Homodyne detection with a sufficiently strong LO allows this signal to be measured down to the quantum limit, rather than being swamped by Johnson noise [48].

Given  $x_n, w_{mn} \in [-1, 1]$  as before, the comb line amplitudes input to the homodyne detector, normalized to photon number, are  $a_w = \alpha_w w_{mn}$  and  $a_x = \alpha_x x_n$  (where  $N_{LO} = |\alpha_x|^2$  is the LO strength, i.e. the number of LO photons per MAC). In the weak-signal limit  $\alpha_w \ll \alpha_x$ , the differential and total charge accumulated at the detector pair, per time step, is (Table I):

$$Q_{\text{diff}} = 2\alpha_w \alpha_x w_{mn} x_n, \quad Q_{\text{tot}} = \alpha_x^2 |x_n|^2 \quad (4)$$

In communications, coherent formats are often associated with higher energy per bit: the higher spectral efficiency and quantum-limited SNR come at the expense of costly digital signal processing (DSP), accounting for about 50% of the link power [49]. For coherent Netcast to be competitive in energy efficiency, it is necessary to use a DSP-free receiver techniques [50] based on coherence cloning of combs [43]–[46], where the cost of comb stabilization is amortized by the number  $M$  of wavelength channels. Such techniques will become more commonplace as microcomb technology and data-center coherent links continue to develop.

#### IV. ENERGY CONSUMPTION AND NOISE

Since the total number of operations scales as  $O(N^2)$ , when running on a single client, Netcast does not yield an improvement in *total* energy efficiency compared to running the DNN digitally. However, the client-side power consumption is reduced significantly—since as discussed previously, the electrical energy consumption for an  $N \times N$  layer scales as  $O(N)$ , which translates to an energy per MAC scaling of  $O(N^{-1})$ . Figures based on current technology ( $O(1)$  pJ/sample for modulation, DAC, and ADC [41], [51]–[54], see also discussions in [19], [27], [55], [56]), suggest fJ/MAC (client side) performance with matrix sizes  $N \gtrsim 100$  (achievable with current hardware [36]), several orders of magnitude below the current (system-level) CMOS state of the art [57]–[59].

One should also consider the optical energy consumption, i.e. the energy of the optical weight signal transmitted over the link, as this is often tied to fundamental limits on the performance of photonic hardware [41], [55], [60]. The photon number sets the signal-to-noise ratio of the client's detectors, with the measured detector charge taking the form:

$$Q_m = \sum_n Q_{\text{diff},mn} + N(0, \sigma_Q^2), \quad \sigma_Q^2 = \underbrace{\frac{kTC}{e^2}}_{\text{Johnson}} + \underbrace{\sum_n Q_{\text{tot},mn}}_{\text{shot}} \quad (5)$$

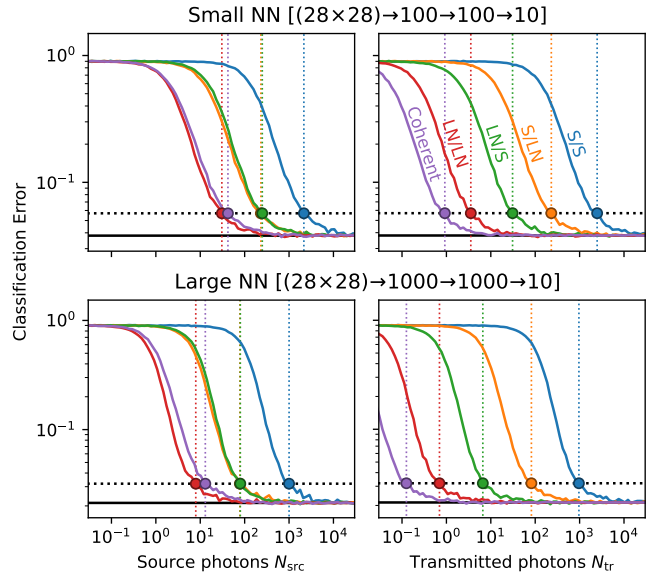


Fig. 3. Effect of shot noise on accuracy of MNIST fully-connected DNNs. Left column: dependence on  $N_{\text{src}}$  (same value used for all layers). Right column: dependence on  $N_{\text{tr}}$ . Circles denote the point at which the DNN classification error increases to  $1.5\times$  over its noiseless value.

The measured matrix-vector product  $y_m$  is proportional to  $Q$ ; thus noise manifests as a Gaussian error term in the analog matrix-vector multiplication

$$y_m = \sum_n w_{mn} x_n + N(0, \sigma^2), \quad \sigma = \sqrt{\sigma_J^2 + \sigma_S^2} \quad (6)$$

where the terms  $\sigma_J$  and  $\sigma_S$  correspond to Johnson (kTC) and shot noise (normalized to the signal). Both terms depend on the optical power [55], proportional to the number of photons per MAC, which we can define in two ways: (1) in terms of the source photons before modulation  $N_{\text{src}}$ , or (2) in terms of the transmitted photons after modulation at the server  $N_{\text{tr}}$ . For the simple differential-signaling transmitter,  $N_{\text{tr}} = N_{\text{src}}$ , but for the low-noise and coherent designs, it can be much smaller for networks with many small weights (see Table I). Since the server's optical output can be amplified before transmission,  $N_{\text{tr}}$  is likely the more practically relevant energy metric. In terms of  $N_{\text{src}}, N_{\text{tr}}$ , the noise amplitudes scale as:

$$\sigma_J^2 = \frac{kTC/e^2}{N_{\text{src}}^2}, \quad \sigma_S^2 = F_{\text{src}} \frac{N}{N_{\text{src}}} = F_{\text{tr}} \frac{N}{N_{\text{tr}}} \quad (7)$$

The Johnson noise term is self-explanatory. In the shot noise term, we observe an additional constant of proportionality ( $F_{\text{src}}, F_{\text{tr}}$ , see Table I), which depends on the transmitter and detector design, since different designs have different  $Q_{\text{tot}}$ , which sets the shot noise. These dimensionless constants quantify the noise reduction of the coherent and low-noise schemes relative to the simple schemes and are  $\ll 1$  if most of the inputs or weights are small.

Naturally, these noise terms will set a lower limit to the (optical) energy consumption of the Netcast system. We can quantify this by running simulations of benchmark DNNs at a range of power levels to find the cutoff point. As a

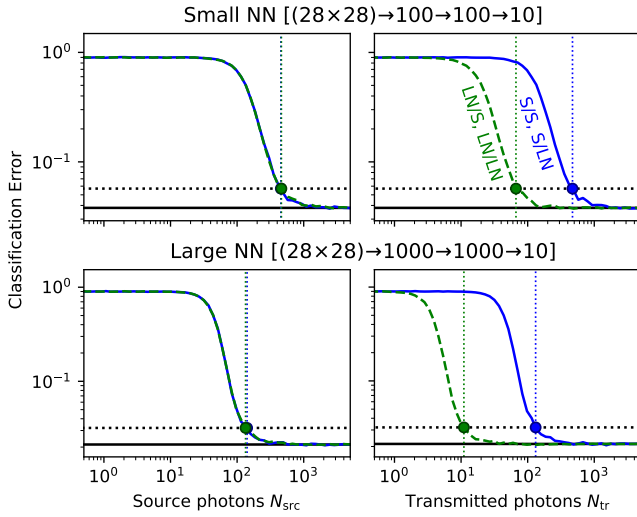


Fig. 4. Effect of Johnson noise on DNN accuracy ( $C = 0.1$  pF). Since  $\sigma_J$  depends only on  $N_{\text{src}}$ , the curves in the left column coincide.

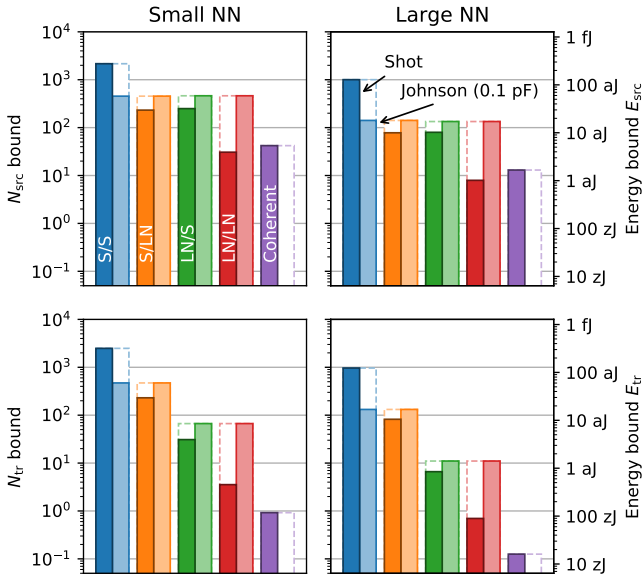


Fig. 5. Summary of lower limits to photon number per MAC (either  $N_{\text{src}}$  or  $N_{\text{tr}}$ ) due to shot noise (Fig. 3) and Johnson noise (Fig. 4).

benchmark, here we consider two three-layer fully-connected DNNs trained on the MNIST dataset: a “small” DNN of size  $(28 \times 28) \rightarrow 100 \rightarrow 100 \rightarrow 10$  (i.e. a network with a  $28 \times 28$  input image and a size-10 output, with two hidden layers of 100 neurons each) and a “large” DNN of size  $(28 \times 28) \rightarrow 1000 \rightarrow 1000 \rightarrow 10$  (1000-neuron hidden layers, see Ref. [41] for details). To simplify the analysis, the effects of Johnson and shot noise are studied separately.

Fig. 3 considers shot noise and plots the DNN error rate as a function of photon number. As discussed above, there are two ways to count photons: at the source  $N_{\text{src}}$  (left column) and at the transmitter output  $N_{\text{tr}}$  (right column). We use the

same  $N_{\text{src}}$  (resp.  $N_{\text{tr}}$ ) for each layer so that there is only one parameter to vary (rather than three), although layerwise optimization can yield better energy efficiency [60]. The expected behavior is observed: random guessing for  $N \ll 1$ , noiseless “digital” accuracy for  $N \gg 1$ , and a crossover that corresponds to the standard quantum limit (SQL) for Netcast running these DNNs. The SQLs for the small and large DNNs differ by a factor of 2–5, similar to the trend observed for output-stationary photoelectric-multiplication [41]. As expected in Sec. III, the quantum limit in the simple configuration (S/S) is quite poor ( $\gtrsim 10^3$  photons/MAC), but the low-noise and coherent schemes have much better sensitivity, the SQL reduced up to  $10^2 \times$  relative to  $N_{\text{src}}$  and  $10^4 \times$  relative to  $N_{\text{tr}}$ . These reductions correlate with the factors  $F_{\text{src}}$ ,  $F_{\text{tr}}$  from Table I.

Fig. 4 performs a similar analysis for Johnson noise, which is only applicable to incoherent models. Johnson noise scales with readout amplifier input capacitance, which here we set to a conservative value of  $C = 0.1$  pF [48], [61]. Note that, per Eq. (7), Johnson noise depends only on  $N_{\text{src}}$ ; therefore, the curves of all designs overlap in the left column. Relative to  $N_{\text{tr}}$ , the noise depends only on the transmitter type (S or LN), not the receiver. Therefore, there are only two distinct cases when varying  $N_{\text{tr}}$ . We find a bound of  $N_{\text{src}} = 430$  (resp. 130) for the small (resp. large) DNN in the simple-transmitter case. The low-noise transmitter can reduce the  $N_{\text{tr}}$  bound by about  $10 \times$ , which makes sense because  $\langle |w_{mn}| \rangle \approx 0.1$  for these neural networks.

From these figures, we now have lower bounds to the photon number (or equivalently optical energy) per MAC. Putting this all together, Fig. 5 lists these bounds for each design (S/S, S/LN, LN/S, LN/LN, coherent), noise source (Johnson, shot), and accounting method (source power, transmitted power). Several observations from this figure are worth emphasizing:

- 1) The general ordering from least to most energy-efficient is: S/S < S/LN < LN/S < LN/LN < Coherent.
- 2) The efficiency gains are most pronounced relative to  $N_{\text{tr}}$ .
- 3) S/LN and LN/S have similar performance relative to  $N_{\text{src}}$ , but LN/S is much better relative to  $N_{\text{tr}}$ . Therefore, if we must economize and can only make one device low-noise, it should be the transmitter.
- 4) Among the incoherent schemes, only S/S is shot-noise limited (at  $C = 0.1$  pF). S/LN and LN/S see roughly equal contributions from both noise sources, while LN/LN is strongly Johnson-noise limited. This means that there is little reason to go from LN/S to LN/LN because both are bottlenecked by the (same) Johnson noise bound. Reduced readout capacitance, detector avalanching, or input pre-amplification will be needed to reap the benefits of LN/LN’s lower shot noise.
- 5) The coherent scheme is consistently the best, even in the absence of Johnson noise. The large NN here can operate at an optical energy of  $\approx 15$  zJ/MAC, lower than the 50–100 zJ/MAC predicted in Ref. [41] and the 250 zJ/MAC achieved in Ref. [62]. High-fidelity computation at  $< 1$  photon per MAC is possible because the computation result is the sum over many MACs, which can maintain an acceptable SNR even if the SNR of individual MACs

is below unity [27], [62], corresponding to an effective bit precision [63] far below the  $\sim 8$  bits typically required for digital DNNs.

## V. THROUGHPUT AND CROSSTALK

If the client operates as a matrix-vector multiplier (as shown in Figs. 1-2), it will perform one MAC per weight received; thus the client's throughput is fundamentally limited by the link. We can also envision matrix-matrix clients with on-chip fan-out after the PSR; this increases the maximum throughput by a constant factor (i.e.  $k$  MACs per weight) at the expense of complexity (receiver circuit is duplicated  $k$  times over); nevertheless, link bandwidth still places a limit on throughput in this case. Fundamentally, the channel capacity of an optical link is limited by crosstalk. Since time and frequency are non-commuting operators, the time-frequency bins of Fig. 1(a) are actually non-orthogonal, which will lead to inevitable crosstalk between the matrix elements. This crosstalk ultimately limits the weight throughput of the channel.

For clarity, this section is divided into two parts. Sec. V-A derives a simplified, analytic estimate for the crosstalk and the bounds this places on throughput. For completeness, Sec. V-B considers the exact model for a specific hardware implementation (ring-based modulators, TIFS integration), which agrees with Sec. V-A to within a factor of  $2.5\times$ .

### A. Analytic Estimate

First, we create a simplified model in order to derive an estimate for the crosstalk. For concreteness we focus on ring-based modulators and multiplexers (Fig. 2(b-c)). The crosstalk in this case takes two forms and can be estimated analytically:

- 1) *Temporal crosstalk*. This arises from the finite photon lifetime in the ring modulators and their finite  $RC$  time constant. Lumping these together, we define an approximate modulator response time  $\tau = \sqrt{1/\kappa^2 + (RC)^2}$ . For optimized modulators,  $RC \approx 1/\kappa$ , so  $\tau \approx \sqrt{2}/\kappa$ . We consider temporal crosstalk of the form  $\chi_t = e^{-T/\tau}$ , where  $T$  is the time between weights. This sets an upper limit on the symbol rate  $R = 1/T$  of the modulators:

$$R \leq \frac{\kappa}{\sqrt{2} \log(1/\chi_t)} = \frac{2\pi f_0}{\sqrt{2} Q \log(1/\chi_t)} \quad (8)$$

where  $f_0$  is the optical carrier frequency and  $Q$  is the ring's  $Q$ -factor.

- 2) *Frequency crosstalk*. We will inevitably have crosstalk between channels of the WDM receiver (even if we had a "perfect WDM", the transmitter rings would have frequency crosstalk too). This is set by the Lorentzian lineshape  $\chi_\omega = (\kappa/2)^2 / (\Delta\omega^2 + (\kappa/2)^2)$ , where  $\Delta\omega$  is the WDM channel spacing. In the low-crosstalk case  $\Delta\omega \gg \kappa$ , this gives a minimum channel spacing:

$$\Delta\omega \geq \frac{\kappa}{2\sqrt{\chi_\omega}} = \frac{2\pi f_0}{2Q\sqrt{\chi_\omega}} \quad (9)$$

To obtain a model for the effect of crosstalk, note that the detector charge  $Q_m$  is a bilinear function of the weight signal  $w(t) \leftrightarrow w_{mn}$  and the activation signal  $x(t) \leftrightarrow x_n$ . The most

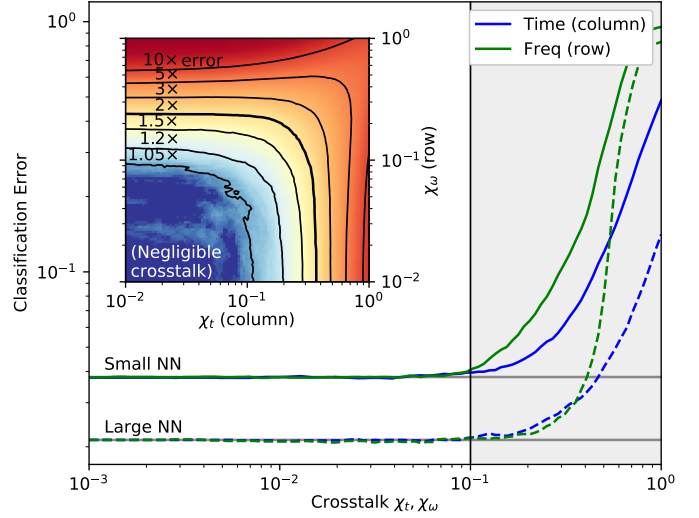


Fig. 6. Effect of crosstalk on MNIST DNN classification accuracy. Crosstalk degrades the neural network when  $\chi_t, \chi_\omega \gtrsim 0.1$ . Inset: classification error in the presence of joint (time plus frequency) crosstalk for the small DNN.

general bilinear form is:  $Q_m = \sum_{m',nn'} Y_{mm',nn'} w_{m'n'} x_n$ . The form of the tensor  $Y$  is subject to a number of symmetries. First,  $Q_m$  is the charge accumulated after time integration, so time-translation symmetry should be respected:  $Y_{mm',nn'} = Y_{mm',(n+p)(n'+p)}$ . Likewise, assuming the demultiplexer's frequency filters are the same for each channel, we also have frequency-translation symmetry:  $Y_{mm',nn'} = Y_{(m+p)(m'+p),nn'}$ . Altogether, this means that the bilinear form reduces to convolution:

$$Q_m = \sum_{pq,n} X_{pq} w_{m+p,n+q} x_n \quad (10)$$

$X_{pq}$  (normalized to  $X_{00} = 1$ ) is the crosstalk matrix. In useful cases, crosstalk is weak and the nearest-neighbor terms dominate: these are (1) the temporal (column) crosstalk ( $X_{0,1}, X_{0,-1}$ ) and (2) the frequency (row) crosstalk ( $X_{1,0}, X_{-1,0}$ ). Often, the crosstalk is also symmetric ( $X_{p,q} = X_{-p,-q}$ ), so there are only two independent parameters:  $\chi_t = X_{0,1} = X_{0,-1}$  and  $\chi_\omega = X_{1,0} = X_{-1,0}$ .

Crosstalk must be sufficiently low for the DNN to function accurately. Since Netcast relies on analog signals, tolerance may be more strict than in a comparable communications system. Ref. [64] analyzed temporal crosstalk for simple MNIST DNNs [41] and AlexNet [65] and found that  $\chi_t \lesssim 0.05$  is usually sufficient. As Fig. 6 shows, spatial and joint crosstalk have a similar threshold; setting  $\chi_t = \chi_\omega \equiv \chi$ , the channel capacity will be bounded by:

$$C = R \frac{2\pi B}{\Delta\omega} \leq \frac{2\pi\sqrt{2}\chi}{\log(1/\chi)} B \equiv C_0 B \quad (11)$$

Here  $B$  is the bandwidth (in Hz) and  $C_0$  is the maximum normalized symbol rate (spectral efficiency, units 1/Hz-s). Table II shows the capacity as a function of crosstalk, both as a normalized rate and assuming use of the full C-band (1530–1565 nm,  $B = 4.4$  THz), which can be converted to

TABLE II  
ESTIMATE OF MAXIMUM LINK BANDWIDTH AS A FUNCTION OF CROSSTALK.

Crosstalk $\chi$	Symbol rate $C_0$	Capacity $C$ (C-band)	$\times 8$ b/wt
0.1	1.22	5.3 Twt/s	43 Tbps
0.05	0.66	2.9 Twt/s	23 Tbps
0.01	0.19	850 Gwt/s	6.8 Tbps
0.005	0.12	520 Gwt/s	4.2 Tbps
0.001	0.04	180 Gwt/s	1.2 Tbps

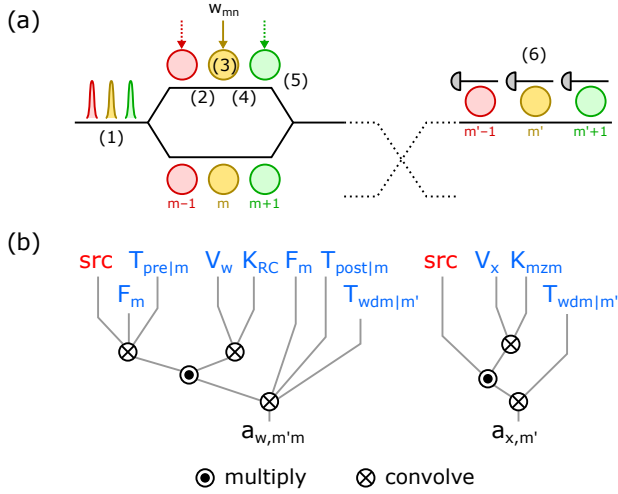


Fig. 7. (a) Path of the optical field as it passes from the weight-server source to the client detector array. The six steps are: initialization at source, pre-filtering by rings  $m' < m$ , modulation by ring  $m$ , output filtering by ring  $m$ , post-filtering by rings  $m' > m$ , and wavelength demultiplexing. (b) Computation of detector-side fields  $a_w(\omega|m'm)$  and  $a_x(\omega|m'm)$ .

an equivalent digital data capacity, assuming 8-bit weights. For reasonable crosstalk values, the data rates are comparable to those achieved with High Bandwidth Memory (HBM) in workstation GPUs (6–12 Tbps [66]). Even at these high data rates ( $\sim$  Twt/s), the sub-fJ/wt optical energy requirements in Fig. 5 indicate that accurate inference is expected even with sub-mW *total* optical power, in the case of a lossless link. For a lossy link, the transmitted power will be larger by a factor  $1/\eta$  where  $\eta$  is the transmission loss, making the low-noise / coherent architectures in Sec. IV a compelling option.

### B. Full Model

A full model for crosstalk is always hardware-dependent. In this section, we study a particular configuration—the coherent TIFS scheme where server-side modulation and client-side multiplexing are performed with microring resonators (Fig. 2(c)). To simplify the math, we assume that the modulators operate in the small-signal (linear) regime, as the addition of modulator nonlinearity is unlikely to affect the magnitude of the crosstalk. Under these assumptions, the weight server output field  $a_w(t)$  and the client LO output  $a_x(t)$  are linear functions of  $w_{mn}$  and  $x_n$ , respectively; as a result, the detector signal will be bilinear in  $w_{mn}$  and  $x_n$ . The symmetry assumptions discussed in Sec. V-A lead to a convolutional crosstalk form Eq. (10), namely  $Q_m = \sum_{pq,n} X_{pq} w_{m+p,n+q} x_n$ .

It remains to compute the crosstalk kernel  $X_{pq}$ . As before, we will focus here on dominant nearest-neighbor terms. We find  $X_{pq}$  by following the field as it passes from source to detector, in the presence of a *single* data pulse  $w_{mn}$  (the overall field is a linear combination of such contributions). This is a sequence of six steps, illustrated in Fig. 6:

- 1) *Initialization*. We start with a frequency comb so that the input field consists of a discrete sum of comb lines:  $a^{(1)}(\omega) = \sum_{m'} \delta(\omega - m'\Omega)$
- 2) *Pre-filtering (rings  $m' < m$ )*. The field is divided into two paths in the WDM-MZM. These paths impart opposite perturbations, so it is sufficient to consider only the top path. The light passes through an array of unperturbed rings. Assuming critical coupling (which makes sense given the tradeoff between speed and modulation amplitude [67], and the added robustness to MZI imperfections [68]). The transfer function for a critically coupled ring is given by  $T(\Delta\omega) = -i\Delta\omega/(\kappa - i\Delta\omega)$ . As a result, the field at this stage is:

$$a^{(2)}(\omega|m) = \left( \prod_{m' < m} T(\omega - m'\Omega) \right) a^{(1)}(\omega) = \sum_{m'} T_{pre}(m'\Omega|m) \delta(\omega - m'\Omega) \quad (12)$$

- 3) *Modulator (ring  $m$ )*. The modulator's internal field is obtained by solving the equations:

$$\begin{aligned} \dot{a}(t) &= (-\kappa - i\Delta(t))a(t) - \sqrt{\kappa}a_{in}(t) \\ a_{out}(t) &= \sqrt{\kappa}a(t) + a_{in}(t) \end{aligned} \quad (13)$$

Here  $\Delta(t)$ , the detuning induced by the signal, is treated in the linear regime as a perturbation. The field in the ring can be expanded to a constant and perturbed term:  $a^{(3)}(t) + \delta a^{(3)}(t)$  (or  $a^{(3)}(\omega) + \delta a^{(3)}(\omega)$ ). The unperturbed part is:

$$a^{(3)}(\omega|m) = -\frac{1}{\sqrt{\kappa}} \frac{\kappa}{\kappa - i(\omega - m\Omega)} a^{(2)}(\omega|m) \quad (14)$$

- 4) *Modulator Perturbation*. The equation for the perturbed part is:

$$\delta \dot{a}(t) = (-\kappa - im\Omega)\delta a(t) - \underbrace{i\Delta(t)a(t)}_{+\kappa S(t)} \quad (15)$$

where we have defined the source term

$$\begin{aligned} S(t|m) &= \kappa^{-1}\Delta(t)a^{(3)}(t|m) \\ S(\omega|m) &= \kappa^{-1}[\Delta(\omega) \otimes a^{(3)}(\omega|m)] \end{aligned} \quad (16)$$

and the detuning  $\Delta$  is the modulator input waveform  $V_w(t)$  passed through its RC filter  $K_{RC}(t)$ :

$$\Delta(t) = [V_w \otimes K_{RC}](t) \Leftrightarrow \Delta(\omega) = V_w(\omega)K_{RC}(\omega) \quad (17)$$

With  $S(\omega|m)$  in hand, we solve Eq. (15) to find  $\delta a^{(3)}(\omega|m) = F(\omega - m\Omega)S(\omega|m)$  with the kernel  $F(\omega)$  defined in Eq. (14).



We only care about the perturbation term from here on, since the unperturbed field cancels out due to the MZM's dual drive. Since there is no perturbation term in the modulator input, the perturbation to the modulator output  $\delta a^{(4)}$  is just:

$$\delta a^{(4)}(\omega|m) = \sqrt{\kappa} \delta a^{(3)}(\omega|m) = \sqrt{\kappa} F(\omega - m\Omega) S(\omega|m) \quad (18)$$

- 5) *Post-filtering (rings  $m' > m$ ).* The perturbed field passes through the rest of the rings and is accordingly filtered. As mentioned earlier, the unperturbed term is cancelled by the symmetry of the WDM-MZM, so we can write  $a^{(5)}$  instead of  $\delta a^{(5)}$  from here on.

$$a^{(5)}(\omega|m) = \left( \prod_{m' > m} T(\omega - m'\Omega) \right) \delta a^{(4)}(\omega|m) \quad (19)$$

$T_{\text{post}}(\omega|m)$

- 6) *Demultiplexing.* Let's consider detector  $m'$ . After mixing with the local oscillator, the field passes by all rings with  $m'' < m'$  and is passed to the drop port of ring  $m'$ , where it goes into a detector. The amplitude in this detector (denoted  $a_w$  because it originates from the weight signal) will be:

$$\begin{aligned} a_w^{(6)}(\omega|m'm) &= \left[ F(\omega - m'\Omega) \prod_{m'' < m'} T(\omega - m''\Omega) \right] a^{(5)}(\omega|m) \\ &= \underbrace{\left[ F(\omega - m'\Omega) \prod_{m'' < m'} T(\omega - m''\Omega) \right]}_{T_{\text{wdm}}(\omega|m')} a^{(5)}(\omega|m) \end{aligned} \quad (20)$$

Note that, for an infinite array of equally spaced frequencies, by symmetry  $a_w^{(6)}(\omega|m'm)$  depends only on the difference index  $(m' - m)$ .

Similarly, we can work through the local oscillator. Here a broadband MZM is used. The input waveform  $V_x(t)$  is convolved by the MZM's filter  $K_{\text{mzm}}(t)$  to produce the modulation amplitude  $\theta(t)$  (here assuming  $\theta \ll 1$ ). This is multiplied by the input frequency comb (same as  $a^{(1)}(\omega)$ ) and sent through the same client-side WDM filter. The final result (in frequency space) is:

$$\begin{aligned} a_x^{(6)}(\omega|m') &= T_{\text{wdm}}(\omega|m') \left( (V_x(\omega) K_{\text{mzm}}(\omega)) \otimes \sum_m \delta(\omega - m\Omega) \right) \end{aligned} \quad (21)$$

Given the form Eq. (10), the crosstalk element  $X_{pq}$  is the interference at detector  $m$  between the signal from  $x_n$  (pulse at the current time step) and the signal from  $w_{m+p, n+q}$  (pulse  $q$  time steps in the future, from modulator  $m+p$ ). This is:

$$X_{pq} \propto \text{Re} \left[ a_x^{(6)}(\omega|m) a_w^{(6)*}(\omega|m, m+p) e^{iq\omega T} \right] \quad (22)$$

These matrix elements depend on many variables including the pulse shapes  $V_{x,w}(t)$ , the RC time constant, the modulator and WDM photon lifetimes, etc. For simplicity, here we consider the case of (1) square-wave  $V_{x,w}$  with duty cycle  $\frac{1}{2}$ , (2)  $RC = \kappa$  for modulator rings, and (3) identical  $\kappa$  for modulator and WDM rings. These parameters set, the matrix elements  $X_{pq}$  depend only on the time- and frequency-spacing

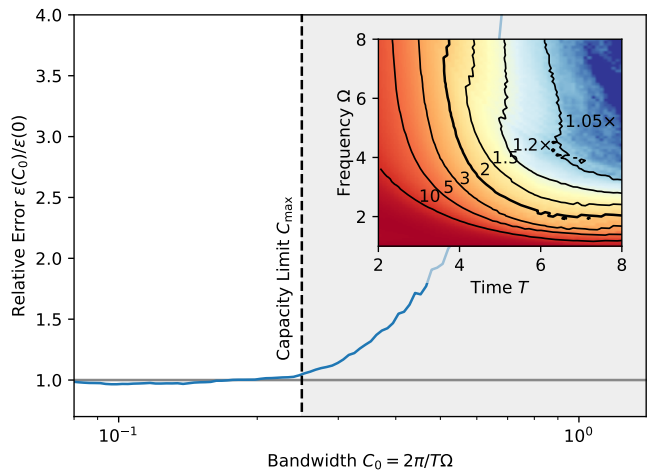


Fig. 8. Bandwidth-accuracy tradeoff for the microring-based Netcast implementation studied in Sec. V-B. The classification error shows a noticeable jump beyond the capacity limit  $C_{\text{max}} \approx 0.25$ . Inset: relative error as a function of time- and frequency-spacing  $(T, \Omega)$ , where the capacity is given by  $C_0 = 2\pi/T\Omega$ .

$(T, \Omega)$ . Given the crosstalk matrix, we compute the MNIST classification accuracy (small NN) as a function of  $(T, \Omega)$ , from which one can derive the optimal accuracy as a function of the capacity  $C_0 = 2\pi/T\Omega$ . This is plotted in Fig. 8. The observed capacity limit  $C_{\text{max}} = 0.25$  is within a factor of 2.5 $\times$  of our analytic estimate obtained in Table II. It should not be too surprising that this is somewhat smaller than the analytic value, as the model used here contains a larger number of bandwidth-limiting factors that can induce additional crosstalk; moreover, the variable choices above (square waves,  $RC = \kappa$ , etc.) could likely be further optimized.

## VI. CONCLUSION

As computing moves to the edge, optics can open up new possibilities to deliver high performance while still meeting strict SWaP constraints. In previous work, we introduced [26] and experimentally demonstrated [27] Netcast, a photonic server-client architecture that leverages unique advantages of optics—the high bandwidth of optical links, support for WDM, wavelength-parallel modulation, and analog integration detection—to split the DNN inference problem into two complementary tasks: weight encoding at the server and lightweight optical postprocessing at the client. This scheme pushes the energy- and memory-intensive tasks to the server, significantly easing pressure on the client's SWaP constraints.

This paper has analyzed the limits to two factors that govern the performance of Netcast: energy efficiency and throughput. By pushing the weight retrieval problem to the server, this protocol allows the electrical energy consumption for a MVM to be reduced from  $O(N^2)$  to in principle  $O(N)$ . Another important consideration is the optical energy, particularly for situations employing large-scale fan-out to many clients or deployment over long-distance links. Optical energy consumption is closely tied to the need to maintain a sufficient SNR in the presence of Johnson and shot noise. We

analyzed five unique server-client configurations which offer tradeoffs between hardware complexity and sensitivity to low optical powers. Numerical simulations reveal that the simplest (differential signaling) design requires  $> 10^3$  photons/MAC for accurate inference, while the most complex (coherent detection) can function with as low as 0.1 photons/MAC.

Throughput of the Netcast client is limited by the delivery of optical weights. Since the weights are encoded in the analog domain, time- and frequency-domain crosstalk pose a fundamental limit to throughput. We have derived analytic expressions for these limits that show Netcast supports bandwidths comparable to high-end GPU HBM, provided the full optical C-band is used. A more detailed physical model agrees roughly with these estimates. Improvements in throughput are possible using coherent detection (a  $4\times$  factor due to use of quadrature and polarization diversity), operation beyond the C-band (which may be enabled by advances in frequency combs [43] and novel amplifiers [69]), and spatial multiplexing.

One direction for future study would be to explore the co-design with digital accelerator architectures—specifically, how best can one harness the server-client separation in Netcast to minimize the system-level energy consumption, including not only optics but also DAC/ADC and memory management [70], [71]. In addition, extending Netcast from delocalized inference to delocalized training would greatly increase its usefulness.

The high theoretical performance limits of Netcast support the use of optics in edge-computing situations where the server and client are connected by an optical link. More broadly, they highlight an exciting new possibility for computing and communications: the use of broadband *analog* optical interconnects to accelerate distributed computing tasks. These interconnects may supplement existing digital links, harnessing the innate parallelism of analog optics to enable new computational architectures in DNN inference, training, sensing, data fusion, and distributed intelligence.

#### ACKNOWLEDGMENT

This research was funded by NTT Research Inc. and NSF EAGER (CNS-1946976). A.S. and S.B. are supported by NSF Graduate Research Fellowships. L.B. is supported by an NSERC Postgraduate Fellowship.

R.H. and D.E. are inventors on U.S. patent application 63/084,600 that covers the Netcast computing scheme.

#### REFERENCES

- [1] W. Yu, F. Liang, X. He, W. G. Hatcher, C. Lu, J. Lin, and X. Yang, "A survey on the edge computing for the internet of things," *IEEE Access*, vol. 6, pp. 6900–6919, 2017.
- [2] V. Sze, Y.-H. Chen, T.-J. Yang, and J. S. Emer, "Efficient processing of deep neural networks: A tutorial and survey," *Proceedings of the IEEE*, vol. 105, no. 12, pp. 2295–2329, 2017.
- [3] T. Chen, Z. Du, N. Sun, J. Wang, C. Wu, Y. Chen, and O. Temam, "DianNao: A small-footprint high-throughput accelerator for ubiquitous machine-learning," *ACM Sigplan Notices*, vol. 49, no. 4, pp. 269–284, 2014.
- [4] A. G. Howard, M. Zhu, B. Chen, D. Kalenichenko, W. Wang, T. Weyand, M. Andreetto, and H. Adam, "Mobilenets: Efficient convolutional neural networks for mobile vision applications," *arXiv preprint arXiv:1704.04861*, 2017.

- [5] F. N. Iandola, S. Han, M. W. Moskewicz, K. Ashraf, W. J. Dally, and K. Keutzer, "SqueezeNet: AlexNet-level accuracy with 50x fewer parameters and 0.5 mb model size," *arXiv preprint arXiv:1602.07360*, 2016.
- [6] L. Deng, G. Li, S. Han, L. Shi, and Y. Xie, "Model compression and hardware acceleration for neural networks: A comprehensive survey," *Proceedings of the IEEE*, vol. 108, no. 4, pp. 485–532, 2020.
- [7] J. Lee, L. Mukhanov, A. S. Molahosseini, U. Minhas, Y. Hua, J. Martinez del Rincon, K. Dichev, C.-H. Hong, and H. Vandierendonck, "Resource-efficient convolutional networks: A survey on model-, arithmetic-, and implementation-level techniques," *ACM Computing Surveys*, vol. 55, no. 13s, pp. 1–36, 2023.
- [8] X. Xu, Y. Ding, S. X. Hu, M. Niemier, J. Cong, Y. Hu, and Y. Shi, "Scaling for edge inference of deep neural networks," *Nature Electronics*, vol. 1, no. 4, pp. 216–222, 2018.
- [9] C. Szegedy, V. Vanhoucke, S. Ioffe, J. Shlens, and Z. Wojna, "Rethinking the inception architecture for computer vision," in *Proceedings of the IEEE conference on computer vision and pattern recognition*, 2016, pp. 2818–2826.
- [10] Z. Dai, Z. Yang, Y. Yang, J. Carbonell, Q. V. Le, and R. Salakhutdinov, "Transformer-XL: Attentive language models beyond a fixed-length context," *arXiv preprint arXiv:1901.02860*, 2019.
- [11] O. Krestinskaya, A. P. James, and L. O. Chua, "Neuromemristive circuits for edge computing: A review," *IEEE transactions on neural networks and learning systems*, vol. 31, no. 1, pp. 4–23, 2019.
- [12] S. Ambrogio, P. Narayanan, H. Tsai, R. M. Shelby, I. Boybat, C. Di Nolfo, S. Sidler, M. Giordano, M. Bordini, N. C. Farinha *et al.*, "Equivalent-accuracy accelerated neural-network training using analog memory," *Nature*, vol. 558, no. 7708, pp. 60–67, 2018.
- [13] E. G. Paek and D. Psaltis, "Optical associative memory using Fourier transform holograms," *Optical Engineering*, vol. 26, no. 5, p. 265428, 1987.
- [14] N. J. New, "Reconfigurable optical processing system," Mar. 14 2017, US Patent 9,594,394.
- [15] Y. Shen, N. C. Harris, S. Skirlo, M. Prabhu, T. Baehr-Jones, M. Hochberg, X. Sun, S. Zhao, H. Larochelle, D. Englund *et al.*, "Deep learning with coherent nanophotonic circuits," *Nature Photonics*, vol. 11, no. 7, p. 441, 2017.
- [16] M. Prabhu, C. Roques-Carmes, Y. Shen, N. Harris, L. Jing, J. Carolan, R. Hamerly, T. Baehr-Jones, M. Hochberg, V. Ćeperić *et al.*, "Accelerating recurrent ising machines in photonic integrated circuits," *Optica*, vol. 7, no. 5, pp. 551–558, 2020.
- [17] A. N. Tait, T. F. Lima, E. Zhou, A. X. Wu, M. A. Nahmias, B. J. Shastri, and P. R. Prucnal, "Neuromorphic photonic networks using silicon photonic weight banks," *Scientific Reports*, vol. 7, no. 1, p. 7430, 2017.
- [18] S. Pai, Z. Sun, T. W. Hughes, T. Park, B. Bartlett, I. A. Williamson, M. Minkov, M. Milanizadeh, N. Abebe, F. Morichetti *et al.*, "Experimentally realized in situ backpropagation for deep learning in photonic neural networks," *Science*, vol. 380, no. 6643, pp. 398–404, 2023.
- [19] L. Bernstein, A. Sludds, C. Panuski, S. Trajtenberg-Mills, R. Hamerly, and D. Englund, "Single-shot optical neural network," *Science Advances*, vol. 9, no. 25, p. eadg7904, 2023.
- [20] M. Y.-S. Fang, S. Manipatruni, C. Wierzynski, A. Khosrowshahi, and M. R. DeWeese, "Design of optical neural networks with component imprecisions," *Optics Express*, vol. 27, no. 10, pp. 14 009–14 029, 2019.
- [21] S. Bandyopadhyay, R. Hamerly, and D. Englund, "Hardware error correction for programmable photonics," *Optica*, vol. 8, no. 10, pp. 1247–1255, 2021.
- [22] R. Hamerly, S. Bandyopadhyay, and D. Englund, "Stability of self-configuring large multiport interferometers," *Physical Review Applied*, vol. 18, no. 2, p. 024018, 2022.
- [23] —, "Accurate self-configuration of rectangular multiport interferometers," *Physical Review Applied*, vol. 18, no. 2, p. 024019, 2022.
- [24] —, "Asymptotically fault-tolerant programmable photonics," *Nature Communications*, vol. 13, no. 1, p. 6831, 2022.
- [25] C. Alexiev, J. C. Mak, W. D. Sacher, and J. K. Poon, "Calibrating rectangular interferometer meshes with external photodetectors," *OSA Continuum*, vol. 4, no. 11, pp. 2892–2904, 2021.
- [26] R. Hamerly, A. Sludds, S. Bandyopadhyay, L. Bernstein, Z. Chen, M. Ghobadi, and D. Englund, "Edge computing with optical neural networks via WDM weight broadcasting," in *Emerging Topics in Artificial Intelligence (ETAI) 2021*, vol. 11804. SPIE, 2021, pp. 55–60.
- [27] A. Sludds, S. Bandyopadhyay, Z. Chen, Z. Zhong, J. Cochrane, L. Bernstein, D. Bunandar, P. B. Dixon, S. A. Hamilton, M. Streshinsky *et al.*, "Delocalized photonic deep learning on the internet's edge," *Science*, vol. 378, no. 6617, pp. 270–276, 2022.

- [28] Z. Zhong, W. Wang, M. Ghobadi, A. Sludds, R. Hamerly, L. Bernstein, and D. Englund, "IoI: In-network optical inference," in *Proceedings of the ACM SIGCOMM 2021 Workshop on Optical Systems*, 2021, pp. 18–22.
- [29] H. Xu and Y. Shi, "Ultra-broadband silicon polarization splitter-rotator based on the multi-mode waveguide," *Optics Express*, vol. 25, no. 15, pp. 18 485–18 491, 2017.
- [30] E. Ciaramella, Y. Arimoto, G. Contestabile, M. Presi, A. D'Errico, V. Guarino, and M. Matsumoto, "1.28 terabit/s (32x40 gbit/s) wdm transmission system for free space optical communications," *IEEE Journal on Selected Areas in Communications*, vol. 27, no. 9, pp. 1639–1645, 2009.
- [31] M. Z. Chowdhury, M. T. Hossain, A. Islam, and Y. M. Jang, "A comparative survey of optical wireless technologies: Architectures and applications," *IEEE Access*, vol. 6, pp. 9819–9840, 2018.
- [32] E. Timurdogan, C. M. Sorace-Agaskar, J. Sun, E. S. Hosseini, A. Biberman, and M. R. Watts, "An ultralow power athermal silicon modulator," *Nature Communications*, vol. 5, p. 4008, 2014.
- [33] V. Stojanović, R. J. Ram, M. Popović, S. Lin, S. Moazeni, M. Wade, C. Sun, L. Alloatti, A. Atabaki, F. Pavanello *et al.*, "Monolithic silicon-photonics platforms in state-of-the-art cmos soi processes," *Optics Express*, vol. 26, no. 10, pp. 13 106–13 121, 2018.
- [34] C. Haffner, D. Chelladurai, Y. Fedoryshyn, A. Josten, B. Baeuerle, W. Heni, T. Watanabe, T. Cui, B. Cheng, S. Saha *et al.*, "Low-loss plasmon-assisted electro-optic modulator," *Nature*, vol. 556, no. 7702, p. 483, 2018.
- [35] M. de Cea, A. Atabaki, and R. Ram, "Energy harvesting optical modulators with sub-attojoule per bit electrical energy consumption," *Nature Communications*, vol. 12, no. 1, pp. 1–9, 2021.
- [36] A. Rizzo, A. Novick, V. Gopal, B. Y. Kim, X. Ji, S. Daudlin, Y. Okawachi, Q. Cheng, M. Lipson, A. L. Gaeta *et al.*, "Massively scalable kerr comb-driven silicon photonic link," *Nature Photonics*, vol. 17, no. 9, pp. 781–790, 2023.
- [37] W. Zhang, C. Huang, H.-T. Peng, S. Bilodeau, A. Jha, E. Blow, T. F. de Lima, B. J. Shastri, and P. Prucnal, "Silicon microring synapses enable photonic deep learning beyond 9-bit precision," *Optica*, vol. 9, no. 5, pp. 579–584, 2022.
- [38] G. Giamougiannis, A. Tsakyridis, M. Moralis-Pegios, C. Pappas, M. Kirtas, N. Passalis, D. Lazovsky, A. Tefas, and N. Pleros, "Analog nanophotonic computing going practical: silicon photonic deep learning engines for tiled optical matrix multiplication with dynamic precision," *Nanophotonics*, vol. 12, no. 5, pp. 963–973, 2023.
- [39] M. Al-Qadasi, L. Chrostowski, B. Shastri, and S. Shekhar, "Scaling up silicon photonic-based accelerators: Challenges and opportunities," *APL Photonics*, vol. 7, no. 2, 2022.
- [40] X. Xu, M. Tan, B. Corcoran, J. Wu, A. Boes, T. G. Nguyen, S. T. Chu, B. E. Little, D. G. Hicks, R. Morandotti *et al.*, "11 tops photonic convolutional accelerator for optical neural networks," *Nature*, vol. 589, no. 7840, pp. 44–51, 2021.
- [41] R. Hamerly, L. Bernstein, A. Sludds, M. Soljačić, and D. Englund, "Large-scale optical neural networks based on photoelectric multiplication," *Physical Review X*, vol. 9, no. 2, p. 021032, 2019.
- [42] R. Hamerly, "The future of deep learning is photonic: reducing the energy needs of neural networks might require computing with light," *IEEE Spectrum*, vol. 58, no. 7, pp. 30–47, 2021.
- [43] Y. Geng, H. Zhou, X. Han, W. Cui, Q. Zhang, B. Liu, G. Deng, Q. Zhou, and K. Qiu, "Coherent optical communications using coherence-cloned kerr soliton microcombs," *Nature Communications*, vol. 13, no. 1, pp. 1–8, 2022.
- [44] J. N. Kemal, J. Pfeifle, P. Marin-Palomo, M. D. G. Pascual, S. Wolf, F. Smyth, W. Freude, and C. Koos, "Multi-wavelength coherent transmission using an optical frequency comb as a local oscillator," *Optics Express*, vol. 24, no. 22, pp. 25 432–25 445, 2016.
- [45] J. K. Jang, A. Klenner, X. Ji, Y. Okawachi, M. Lipson, and A. L. Gaeta, "Synchronization of coupled optical microresonators," *Nature Photonics*, vol. 12, no. 11, pp. 688–693, 2018.
- [46] P. Liao, C. Bao, A. Almaiman, A. Kordts, M. Karpov, M. H. P. Pfeiffer, L. Zhang, F. Alishahi, Y. Cao, K. Zou *et al.*, "Demonstration of multiple kerr-frequency-comb generation using different lines from another kerr comb located up to 50 km away," *Journal of Lightwave Technology*, vol. 37, no. 2, pp. 579–584, 2019.
- [47] P. J. Winzer, D. T. Neilson, and A. R. Chraplyvy, "Fiber-optic transmission and networking: the previous 20 and the next 20 years," *Optics Express*, vol. 26, no. 18, pp. 24 190–24 239, 2018.
- [48] J. F. Tasker, J. Frazer, G. Ferranti, E. J. Allen, L. F. Brunel, S. Tanzilli, V. D'Auria, and J. C. Matthews, "Silicon photonics interfaced with integrated electronics for 9 ghz measurement of squeezed light," *Nature Photonics*, vol. 15, no. 1, pp. 11–15, 2021.
- [49] R. Nagarajan, I. Lyubomirsky, and O. Agazzi, "Low power dsp-based transceivers for data center optical fiber communications (invited tutorial)," *Journal of Lightwave Technology*, vol. 39, no. 16, pp. 5221–5231, 2021.
- [50] J. K. Perin, A. Shastri, and J. M. Kahn, "Coherent data center links," *Journal of Lightwave Technology*, vol. 39, no. 3, pp. 730–741, 2020.
- [51] D. A. Miller, "Energy consumption in optical modulators for interconnects," *Optics Express*, vol. 20, no. 102, pp. A293–A308, 2012.
- [52] A. H. Atabaki, S. Moazeni, F. Pavanello, H. Gevorgyan, J. Notaros, L. Alloatti, M. T. Wade, C. Sun, S. A. Kruger, H. Meng *et al.*, "Integrating photonics with silicon nanoelectronics for the next generation of systems on a chip," *Nature*, vol. 556, no. 7701, p. 349, 2018.
- [53] B. E. Jonsson, "An empirical approach to finding energy efficient ADC architectures," in *Proc. of 2011 IMEKO IWADC & IEEE ADC Forum*, 2011, pp. 1–6.
- [54] S. Cosemans, B. Verhoef, J. Doevenspeck, I. Papiastas, F. Catthoor, P. Debacker, A. Mallik, and D. Verkest, "Towards 10000TOPS/W DNN inference with analog in-memory computing—a circuit blueprint, device options and requirements," in *2019 IEEE International Electron Devices Meeting (IEDM)*. IEEE, 2019, pp. 22–2.
- [55] A. N. Tait, "Quantifying power in silicon photonic neural networks," *Physical Review Applied*, vol. 17, no. 5, p. 054029, 2022.
- [56] C. Cole, "Optical and electrical programmable computing energy use comparison," *Optics Express*, vol. 29, no. 9, pp. 13 153–13 170, 2021.
- [57] M. Horowitz, "Computing's energy problem (and what we can do about it)," in *Solid-State Circuits Conference Digest of Technical Papers (ISSCC), 2014 IEEE International*. IEEE, 2014, pp. 10–14.
- [58] N. P. Jouppe, C. Young, N. Patil, D. Patterson, G. Agrawal, R. Bajwa, S. Bates, S. Bhatia, N. Boden, A. Borchers *et al.*, "In-datacenter performance analysis of a tensor processing unit," in *Computer Architecture (ISCA), 2017 ACM/IEEE 44th Annual International Symposium on*. IEEE, 2017, pp. 1–12.
- [59] A. Reuther, P. Michaleas, M. Jones, V. Gadepally, S. Samsi, and J. Kepner, "Survey and benchmarking of machine learning accelerators," in *2019 IEEE high performance extreme computing conference (HPEC)*. IEEE, 2019, pp. 1–9.
- [60] S. Garg, J. Lou, A. Jain, Z. Guo, B. J. Shastri, and M. Nahmias, "Dynamic precision analog computing for neural networks," *IEEE Journal of Selected Topics in Quantum Electronics*, vol. 29, no. 2: Optical Computing, pp. 1–12, 2022.
- [61] N. Vokić, P. Brandl, K. Schneider-Hornstein, B. Goll, and H. Zimmermann, "10 gb/s switchable binary/pam-4 receiver and ring modulator driver for 3-d optoelectronic integration," *IEEE Journal of Selected Topics in Quantum Electronics*, vol. 22, no. 6, pp. 344–352, 2016.
- [62] T. Wang, S.-Y. Ma, L. G. Wright, T. Onodera, B. C. Richard, and P. L. McMahon, "An optical neural network using less than 1 photon per multiplication," *Nature Communications*, vol. 13, no. 1, pp. 1–8, 2022.
- [63] M. A. Nahmias, T. F. De Lima, A. N. Tait, H.-T. Peng, B. J. Shastri, and P. R. Prucnal, "Photonic multiply-accumulate operations for neural networks," *IEEE Journal of Selected Topics in Quantum Electronics*, vol. 26, no. 1, pp. 1–18, 2019.
- [64] R. Hamerly, A. Sludds, L. Bernstein, M. Prabhu, C. Roques-Carnes, J. Carolan, Y. Yamamoto, M. Soljačić, and D. Englund, "Towards large-scale photonic neural-network accelerators," in *2019 IEEE international electron devices meeting (IEDM)*. IEEE, 2019, pp. 22–8.
- [65] A. Krizhevsky, I. Sutskever, and G. E. Hinton, "Imagenet classification with deep convolutional neural networks," in *Advances in neural information processing systems*, 2012, pp. 1097–1105.
- [66] J. Choquette, O. Giroux, and D. Foley, "Volta: Performance and programmability," *IEEE Micro*, vol. 38, no. 2, pp. 42–52, 2018.
- [67] J. Witzens, "High-speed silicon photonics modulators," *Proceedings of the IEEE*, vol. 106, no. 12, pp. 2158–2182, 2018.
- [68] A. J. Menssen, A. Hermans, I. Christen, T. Propson, C. Li, A. J. Leenheer, M. Zimmermann, M. Dong, H. Larocque, H. Raniwala *et al.*, "Scalable photonic integrated circuits for high-fidelity light control," *Optica*, vol. 10, no. 10, pp. 1366–1372, 2023.
- [69] F. Maes, M. Sharma, L. Wang, and Z. Jiang, "High power BDF/EDF hybrid amplifier providing 27 dB gain over 90 nm in the E+S band," in *Optical Fiber Communication Conference*. Optica Publishing Group, 2022, pp. Th4C–8.
- [70] A. Parashar, P. Raina, Y. S. Shao, Y.-H. Chen, V. A. Ying, A. Mukkara, R. Venkatesan, B. Khailany, S. W. Keckler, and J. Emer, "Timeloop: A systematic approach to dnn accelerator evaluation," in *2019 IEEE international symposium on performance analysis of systems and software (ISPASS)*. IEEE, 2019, pp. 304–315.

- [71] T. Andrulis, R. Chen, H.-S. Lee, J. S. Emer, and V. Sze, "Modeling analog-digital-converter energy and area for compute-in-memory accelerator design," *arXiv preprint arXiv:2404.06553*, 2024.



**Ryan Hamerly** was born in San Antonio, Texas in 1988. In 2016 he received a Ph.D. degree in applied physics from Stanford University, California, for work with Prof. Hideo Mabuchi on quantum control, nanophotonics, and nonlinear optics. In 2017 he was at the National Institute of Informatics, Tokyo, Japan, working with Prof. Yoshihisa Yamamoto on quantum annealing and optical computing concepts, and is currently a Senior Scientist at NTT PHI Laboratories and a visiting scientist at MIT, Cambridge, Massachusetts, with Prof. Dirk Englund.



**Zhizhen Zhong** received his Ph.D. and Bachelor degrees in Electronic Engineering from Tsinghua University in 2019 and 2014, respectively. During his graduate studies, he was a visiting Ph.D. student in the CS Department at the University of California, Davis. After finishing his Ph.D., he was a visiting researcher at the network infrastructure team of Meta. He is currently a postdoctoral researcher working with Prof. Dirk Englund at MIT. His current research explores the intersection between applied photonics and networked systems to build next-generation computing infrastructures.



**Alexander Sludds** received his Bachelors of Science and Masters of Engineering in Electrical Engineering and Computer Science from MIT in 2018 and 2019. As a graduate student with Prof. Dirk Englund at MIT, he focused on the creation of novel CMOS photonic computing and interconnect solutions to enable 1000 $\times$  improvement over existing commercial technology in the datacenter and edge. He received his Ph.D. in 2023 and is currently a photonic architect at Lightmatter.



**Liane Bernstein** received her Bachelor of Engineering from Polytechnique Montreal in 2016, specializing in Photonics. In 2018, she earned her Master of Science in Electrical Engineering and Computer Science at MIT for "Ultrahigh-Resolution, Deep-Penetration Spectral-Domain Optical Coherence Tomography" in Prof. Andy Yun's group. She then developed both theoretical descriptions as well as experimental demonstrations of optical deep neural networks in Prof. Dirk Englund's group at MIT, where she received her Ph.D. in 2024. She is currently an optical engineer at QuEra Computing.



**Saamil Bandyopadhyay** received his S.B. in Electrical Engineering and M.Eng. in Electrical Engineering and Computer Science from MIT in 2017 and 2018, respectively. He was a recipient of the NSF Graduate Research Fellowship and studied in the group of Prof. Dirk Englund at MIT. He received his Ph.D. in 2023 and is currently a postdoctoral fellow with NTT Research and a visiting scientist at MIT, where he works on programmable silicon photonics for artificial intelligence.



**Zaijun Chen** accomplished his Ph.D. degree in Prof. Theodor W. Hänsch's group at Max-Planck Institute of Quantum Optics (MPQ) and LMU Munich in 2019, for work on frequency-comb-based precision spectroscopy with Dr. Nathalie Picqué. In 2020, he worked with Prof. Christian Gross on quantum simulation with cold atoms in optical tweezers in Prof. Immanuel Bloch's group at MPQ. He moved to MIT as a postdoctoral researcher in Prof. Dirk Englund's group in 2021, where his research focus is optical computing for machine learning applications.

He is currently starting his own research group in the Ming Hsieh Department of Electrical and Computer Engineering at University of Southern California.



**Dirk Englund** received his BS in Physics from Caltech in 2002. After a Fulbright fellowship at T.U. Eindhoven, he completed an MS in Electrical Engineering and a PhD in Applied Physics at Stanford University in 2008. After a postdoctoral fellowship at Harvard University, he joined Columbia University as Assistant Professor of E.E. and of Applied Physics. He joined the MIT EECS faculty in 2013. Recent recognitions include the 2011 PECASE, the 2011 Sloan Fellowship in Physics, the 2012 DARPA Young Faculty Award, the 2017 ACS Photonics Young Investigator Award, and the OSA's 2017 Adolph Lomb Medal, a Bose Research Fellowship in 2018, and a 2020 Humboldt Research Fellowship.